Inorganic Chemistry

pubs.acs.org/IC

Article

Structural, Thermodynamic, and Transport Properties of the Small-Gap Two-Dimensional Metal−Organic Kagomé Materials Cu_3(hexaiminobenzene)$_2$ and Ni_3(hexaiminobenzene)$_2$

Tanya Berry, Jennifer R. Morey, Kathryn E. Arpino, Jin-Hu Dou, Claudia Felser, Mircea Dincă, and Tyrel M. McQueen*

Cite This: https://doi.org/10.1021/acs.inorgchem.2c00081

Read Online

ACCESS | Metrics & More | Article Recommendations

ABSTRACT: Metal−organic frameworks (MOFs) provide exceptional chemical tunability and have recently been demonstrated to exhibit electrical conductivity and related functional electronic properties. The kagomé lattice is a fruitful source of novel physical states of matter, including the quantum spin liquid (in insulators) and Dirac fermions (in metals). Small-bandgap kagomé materials have the potential to bridge quantum spin liquid states and exhibit phenomena such as superconductivity but remain exceptionally rare. Here we report a structural, thermodynamic, and transport study of the two-dimensional kagomé metal−organic frameworks $Ni_3(HIB)_2$ and $Cu_3(HIB)_2$ (HIB = hexaiminobenzene). Magnetization measurements yield Curie constants of 0.989 emu K (mol Ni)$^{-1}$ Oe^{-1} and 0.371 emu K (mol Cu)$^{-1}$ Oe^{-1}, respectively, close to the values expected for ideal $S = 1$ Ni^{2+} and $S = {}^1/_2$ Cu^{2+}. Weiss temperatures of −10.6 and −14.3 K indicate net weak mean field antiferromagnetic interactions between ions. Electrical transport measurements reveal that both materials are semiconducting, with gaps (E_g) of 22.2 and 103 meV, respectively. Specific heat measurements reveal a large T-linear contribution γ of 148(4) mJ mol-fu^{-1} K^{-2} in $Ni_3(HIB)_2$ with only a gradual upturn below ∼5 K and no evidence of a phase transition to an ordered state down to 0.1 K. $Cu_3(HIB)_2$ also lacks evidence of a phase transition above 0.1 K, with a substantial, field-dependent, magnetic contribution below ∼5 K. Despite them being superficially in agreement with the expectations of magnetic frustration and spin liquid physics, we ascribe these observations to the stacking faults found from a detailed analysis of synchrotron X-ray diffraction data. At the same time, our results demonstrate that these MOFs exhibit localized magnetism with simultaneous proximity to a metallic state, thus opening up opportunities to explore the connection between the insulating and metallic ground states of kagomé materials in a highly tunable chemical platform.

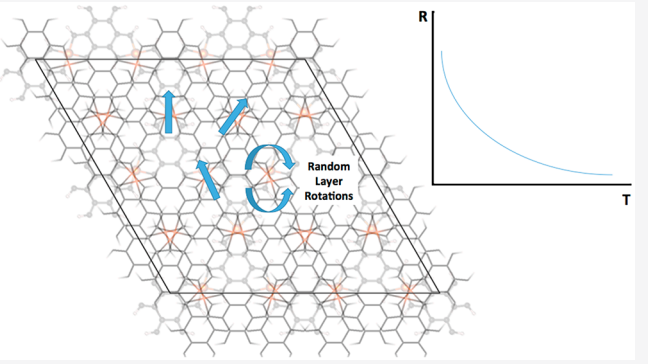

INTRODUCTION

Metal−organic frameworks (MOFs) make up a novel class of materials defined by metal centers connected by organic linkers. The nature of the metal and the organic linkers and the structure dictate the material's properties. Long explored for gas sorption properties, MOFs have recently attracted appreciable attention due to graphene-like structural motifs and tunable electronic properties, including high carrier mobilities and concentrations. This has led to their use in many applications in a variety of fields, including electrocatalysis and electronics (e.g., field-effect transistors).[1−4] This combination of transition metal ions and graphene-like organic motifs provides a high degree of chemical tunability, allowing independent modification of the molecular building blocks to separately tune magnetic (via the transition metals) and bond overlap and metallicity (via the conjugated linkers).

Materials containing a kagomé lattice, consisting of corner-sharing triangles of atoms, have been long explored as candidates for hosting the quantum spin liquid (QSL) state when insulating and magnetic.[5−7] A QSL is a nontrivial magnetic ground state in which there is long-range spin entanglement and the absence of traditional static magnetic order. More recent work has focused on the appearance of Dirac Fermions, or electrons with a linear energy−momentum relationship, in metallic kagomé materials, where the linear

Received: January 12, 2022

dispersion is enforced as a consequence of the underlying geometry. These states are often topological and known to give rise to a giant anomalous Hall effect,[8−10] and, more recently, superconductivity.[11−14]

A persistent chemical challenge with kagomé magnets has been to find a material or a class of materials that can be tuned between the insulating and magnetic and metallic limits, a prerequisite for testing theories such as Anderson's prediction of superconductivity arising from QSL correlations.[15,16]

Recently, a family of MOFs with kagomé lattices and signatures of metallicity have been reported.[17] These materials, $Ni_3(HIB)_2$ and $Cu_3(HIB)_2$, are composed of two-dimensional (2D) kagomé layers in which the transition metal ions form vertices of the kagomé network, held together by planar hexaiminobenzene (HIB) anions (Figure 1). The Ni^{2+} or Cu^{2+}

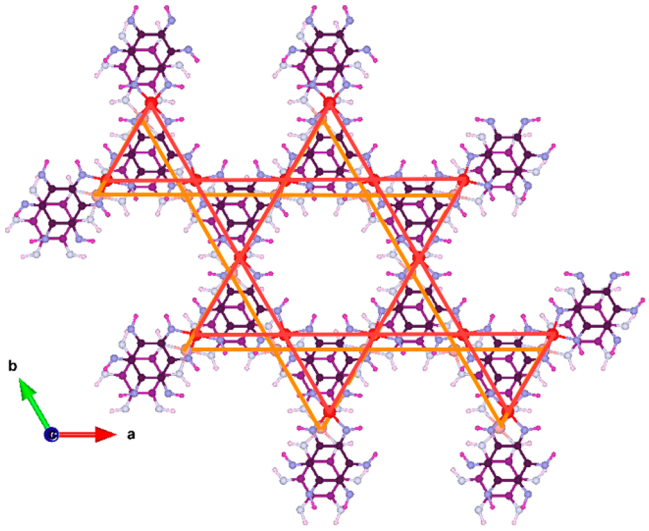

Figure 1. Kagomé network of $M_3(HIB)_2$ depicted with red and orange lines among the metal ions depicted as red circles. The metal ions are magnetic, while the planar HIB molecules provide hopping and superexchange between sites.

ions contain unpaired, localized, magnetic electrons. The HIB anions connect these metal centers and contain a highly delocalized π network of electrons, reminiscent of that found in graphene, providing superexchange coupling and electron hopping between metal sites. We note that due to the π delocalization on the closed shell, anionic ligands, the superexchange interactions between metal centers can be substantially stronger than that expected from atomic distance considerations.[18]

Here we report the result of a combined structural, thermodynamic, and electrical transport study of $Ni_3(HIB)_2$ and $Cu_3(HIB)_2$. Building on prior structural work,[17] we find that both materials contain a significant number of stacking faults arising from 3-fold rotations of individual layers. In addition, we find that the stacking of adjacent layers is similar but not identical for the case of Ni and Cu. Magnetization measurements are consistent with localized Ni^{2+} ($S = 1$) and Cu^{2+} ($S = {}^1/_2$) magnetism at >2 K. The Weiss mean field antiferromagnetic interaction energy scales are weak, −10.6 and −14.3 K, respectively. The lower exchange strength in the case of Cu is consistent with the lower level of square-planar coordination of the Cu ions by HIB. Electrical transport reveals that both materials are small-gap semiconductors, with gaps of 22.2 and 103 meV, respectively. Specific heat measurements show no evidence for a transition to a long-range ordered magnetic state above 0.1 K in either case. There is significant magnetic entropy at low temperatures in the case of Cu, and an anomalously large T-linear contribution in the case of Ni. These observations can be explained as a consequence of the local crystal field environment coupled to the high degree of stacking disorder in these materials.

EXPERIMENTAL SECTION

Synthesis of $Ni_3(HIB)_2$ and $Cu_3(HIB)_2$ Films (HIB = hexaiminobenzene). $Ni_3(HIB)_2$ and $Cu_3(HIB)_2$ films were prepared using a series of synthetic procedures that are explained in detail in the literature.[17] **Warning:** *Compounds 2,4,6-trinitroaniline (TNA) and 1,3,5-triamino-2,4,6-trinitrobenzene (TATB) are very sensitive to mechanical force and highly explosive under alkaline conditions. Both should be handled with extreme caution.* In step 1 [synthesis of 2,4,6-trinitroaniline (TNA)], KNO_3 (0.70 mol) dissolved in H_2SO_4 (100 mL) was added dropwise at 50 °C to a round-bottom flask of 4-nitroaniline (0.14 mol) and H_2SO_4. The round-bottom flask was then heated to 80 °C for 3 h and then 110 °C for 3 h. The reaction mixture was then cooled to room temperature and later placed in an ice/water bath. The precipitates from the cooling were subjected to suction filtration followed by air drying. Recrystallization was achieved with a 0.4 M aqueous HCl solution to give a high yield of glasslike yellow-colored crystals of 2,4,6-trinitroaniline. In step 2 [synthesis of 1,3,5-triamino-2,4,6-trinitrobenzene (TATB)], mixtures of sodium methoxide (0.44 mol) in TNA (0.02 mol) and 4-amino-1,2,4-triazole (ATA) (0.2 mol) in DMSO (300 mL) were combined. This formed an orange-colored suspension that was stirred at room temperature for 3 h. The reaction mixture was then poured into HCl (0.4 M), and then the precipitates were separated via suction filtration, washed in distilled H_2O, and dried. The solids were dissolved in a solution of DMSO and trace amounts of NaOH and were heated at 70 °C. After the mixture was dissolved, it was decanted in a cold HNO_3 (0.4 M) solution. The precipitate was filtered, and deep yellow-colored TATB was obtained. In step 3 [synthesis of hexaaminobenzene (HAB)], TATB (0.012 mol), 10% Pd/C, and pure ethyl acetate were placed in a high-pressure hydrogenation bottle. The reaction container was agitated under H_2 (4.2 bar) for 3 days. The yellowish color of the reactant mixture was no longer observed. Concentrated HCl was mixed under H_2 for 5 h. The solution was filtered under reduced pressure over Celite, and HAB trihydrochloride was afforded. The precipitates were subjected to suction filtration and dried at 70 °C for 2 h under reduced pressure. The crystals were redissolved in deionized H_2O and filtered; a concentrated aqueous HCl solution was added, and the mixture sealed in a freezer. This process again allowed crystallization. The crystals were accumulated through gravity filtration, washed with ethyl acetate, and dried in a furnace to afford a high yield. In step 4a [synthesis of $Ni_3(HIB)_2$ and $Cu_3(HIB)_2$ powders], $Ni(NO_3)_2{\cdot}6H_2O$ and $CuSO_4{\cdot}5H_2O$ (0.11 mmol) were added to different scintillation vials along with 14 M NH_4OH in DMSO and HAB·3HCl (0.072 mmol) in degassed DMSO. The vials were heated at 65 °C for 2 h, and a black precipitate formed. This suspended mixture was centrifuged, decanted, and washed with deionized water and acetone. The solid product was dried under vacuum on a Schlenk line for 10 min.

Stacking Fault Analysis. Prior work reported high-fidelity synchrotron X-ray diffraction data (λ = 0.517045 Å) on $Ni_3(HIB)_2$ and $Cu_3(HIB)_2$ but did not report an analysis of the stacking faults and did not attempt to properly capture the peak intensities or asymmetries.[17] Here we carry out a comprehensive analysis of those data, utilizing quantitative predictions of peak shapes and intensities as implemented in the DIFFaX software suite.[19] To carry out these simulations, we had to modify DIFFaX to support a larger number of atoms per layer than it does by default. We also found it necessary to further modify it to take advantage of multicore processing (https://github.com/tmcqueen-materials/DIFFaX-openmp-patches) to allow

https://doi.org/10.1021/acs.inorgchem.2c00081
Inorg. Chem. XXXX, XXX, XXX−XXX

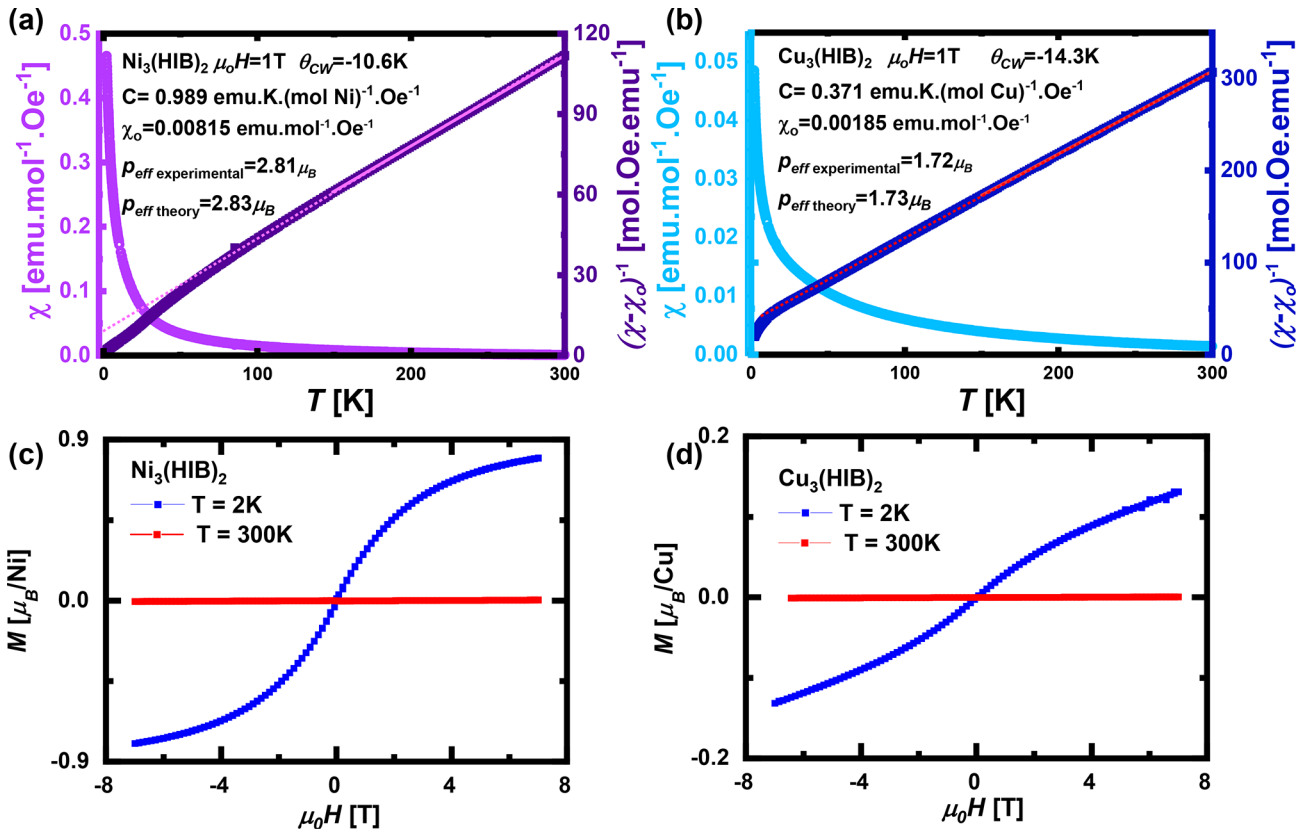

Figure 2. Curie–Weiss analysis of (a) $Ni_3(HIB)_2$ and (b) $Cu_3(HIB)_2$. The data are consistent with $S = 1$ and $S = {}^1/_2$ paramagnetic behavior, respectively, with weak antiferromagnetic interactions. $M(H)$ curves of (c) $Ni_3(HIB)_2$ and (d) $Cu_3(HIB)_2$ show no pronounced features or behavior.

automated refinement of stacking fault parameters by an iterative process as implemented by Materials Automated.[20] Models were constructed starting from the previously reported CIF files, and splitting into individual, symmetry-related, layers using the Python Atomic Simulation Environment, version 3.22.0.[21] Each of the two symmetry-related layers from each compound was recast into a trigonal cell and individually rotated 0°, 120°, and 240° around (0.325, 0.25, 0.0) (layer 1) or (0.125, 0.25, 0.0) (layer 2) to produce three rotation-equivalent versions of each layer. These were then reconstituted in pairs to produce the nine possible configurations for the relative orientations of pairs of layers. The final structural model then consisted of six refinable parameters: an overall scale factor, two in-plane displacement values offsetting layer 2 relative to layer 1 within each layer pair, two in-plane displacement values relating the layers 1 of two successive pairs, and a single transition probability, describing the probability that two adjacent layers adopt an unfaulted (0°) orientation relative to the previous layer. For the sake of simplicity, and because it does not significantly impact the results, all atomic displacement parameters were fixed at $B_{iso} = 1.0$, and known instrumental broadening parameters were included. Finite particle size effects were also included. The result is the stacking fault model described in the text.

Physical Property Measurement. The resistivity and heat capacity of $Ni_3(HIB)_2$ and $Cu_3(HIB)_2$ were measured using a quantum design physical property measurement system (PPMS) equipped with a dilution refrigerator. Temperature-dependent resistivity measurements were performed using a standard four-point probe technique at $\mu_oH = 0$, 3, and 5 T. Specimens were pellets densified at >1000 bar and cut into an approximately rectangular shape ~1–2 mm in length and ~0.1 mm^2 in cross sectional area. Contacts were made using 50 μm Pt wire and Dupont 4922N silver paste. The contact resistance, estimated from pairwise two-probe measurements at room temperature, was estimated to be <100 Ω per contact. Specific heat measurements were performed between 0.1 and 300 K at $\mu_oH = 0$ and 1 T using the semiadiabatic pulse technique with a 1% temperature increase and measurement over three time constants. Each measurement was performed in triplicate. Apiezon N grease was used to ensure suitable thermal coupling, with the addenda collected over the same temperature range. Fits were checked to ensure there was no evidence for the presence of a first-order phase transition. Magnetization data were collected using an MPMS-7T instrument from 2 to 300 K under $\mu_oH = 1$ T and converted to magnetic susceptibility using the approximation $\chi = M/H$. Samples were mounted as fixed pellets in a straw to avoid the preferred orientation.

RESULTS AND DISCUSSION

Magnetic susceptibility measurements for $Ni_3(HIB)_2$ and $Cu_3(HIB)_2$ are shown in panels a and b, respectively, of Figure 2. Curie–Weiss analysis for $Ni_3(HIB)_2$ (Figure 2a) was performed over the temperature range of 150–300 K and yielded a Curie constant C of 0.989 emu K (mol Ni)$^{-1}$ Oe^{-1} and a Θ_{CW} of −10.6 K. The Curie constant is in good agreement with the expected value of 1.0 for a Ni^{2+} ($S = 1$) ion, and the Weiss temperature indicates net antiferromagnetic interactions. This linear fit provides a good description of the data over a wider range than the fit and indicates paramagnetic behavior over the entire measured temperature range with no evidence of magnetic order down to 2 K. The $M(H)$ curves at 300 and 2 K (Figure 2c) are featureless. $Ni_3(HIB)_2$ thus satisfies the canonical condition for frustration: $|\Theta_{CW}|/T_{order} >$ ~55 > 10 [with $T_{order} < 0.2$ K (*vida infra*)].

Similar behavior is found for $Cu_3(HIB)_2$ (Figure 2b). Curie–Weiss analysis was performed at 150–300 K and yielded a Curie constant C of 0.371 emu K (mol Cu)$^{-1}$ Oe^{-1}

https://doi.org/10.1021/acs.inorgchem.2c00081
Inorg. Chem. XXXX, XXX, XXX–XXX

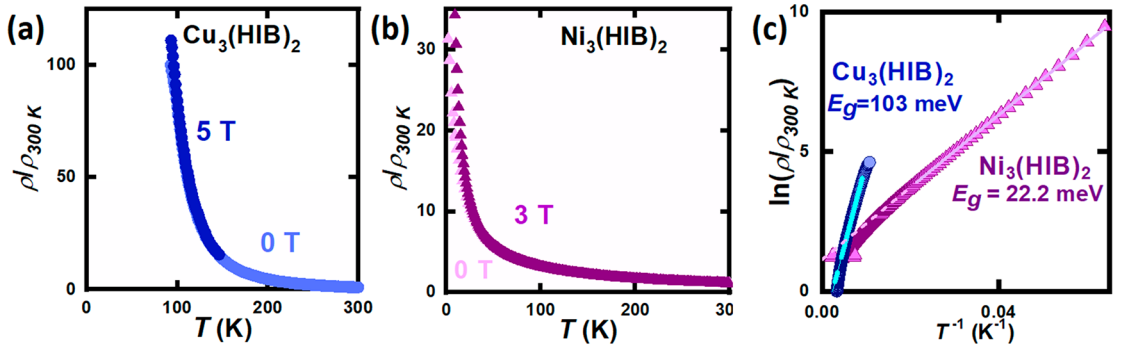

Figure 3. (a) Resistivity of $Cu_3(HIB)_2$ at μ_oH = 0 and 5 T. (b) Resistivity of $Ni_3(HIB)_2$ at μ_oH = 0 and 3 T. (c) Arrhenius fit for bandgap determination of $Cu_3(HIB)_2$ (E_g = 103 meV) and $Ni_3(HIB)_2$ (E_g = 22.2 meV).

and a Θ_{CW} of −14.3 K. The Weiss temperature is negative, indicative of antiferromagnetic interactions. The Curie constant is in good agreement with the expected value of 0.375 for a spin-only $S = {}^1/_2$ moment. It is, however, slightly smaller than the value of ∼0.4 typically found in Cu^{2+} compounds. The origin of this reduced value is likely metal−ligand covalency, expected given the proximity to a metallic state. The Curie−Weiss behavior appears to extend down to the lowest temperature measured, 2 K, with no signatures of magnetic ordering. The $M(H)$ curves at 300 and 2 K (Figure 2d) are similarly featureless. Considering that no magnetic order is observed in specific heat down to 0.2 K (*vida infra*), $Cu_3(HIB)_2$ is also canonically frustrated, with $|\Theta_{CW}|/T_{order}$ > ∼70 > 10. Thus, we find both materials are candidates for magnetic frustration and quantum spin liquid behavior.

Given the color of both materials—black, in sharp contrast with the more usual strongly colored (wide bandgap) QSL candidates—it is natural to explore the electrical properties to see if they can fill the gap between highly insulating and highly metallic kagomés. The existing literature contains contradictory reports of metallic or semiconducting behavior in conductive MOFs, depending on the measurement technique and precise sample form.[17,22,23] The use of noncontact or two-probe measurement configurations, combined with a high contact resistance in most cases, makes the determination of intrinsic properties difficult.[24,25] The analysis is further complicated by the polycrystalline nature of bulk species, because metallic materials have previously been observed to exhibit activated conduction when there are insulating grain boundaries that dominate conduction.[26] Here, careful contact preparation combined with a four-probe technique, which together eliminate the contact resistance contributions, was utilized to re-examine the temperature-dependent resistivity of $Ni_3(HIB)_2$ and $Cu_3(HIB)_2$. The resistivities of both materials increase with a decrease in temperature (Figure 3a,b), consistent with bulk transport dominated by a thermally activated process. The room-temperature resistivities are found to be 30 and 5 × 10^5 Ω cm for $Ni_3(HIB)_2$ and $Cu_3(HIB)_2$ respectively. This semiconducting behavior is in agreement with a prior report that found semiconducting transport in the range of 200−300 K; our data extend this trend to significantly lower temperatures, with higher reliability upon elimination of contact contributions.

An Arrhenius fit, calculated on the basis of the relationship $\ln(\rho_T/\rho_{300\ K}) = 2k_BE_gT^{-1} + b$, where k_B is the Boltzmann constant, E_g is the bandgap, and b is the intercept of the line, used on a linear region in a plot of the natural log of the resistivity normalized to the resistivity at 300 K versus inverse temperature (Figure 3c), gives bandgaps of 22.2 meV for $Ni_3(HIB)_2$ and 103 meV for $Cu_3(HIB)_2$. The magnitudes of these gaps are consistent with the observed resistances at room temperature, assuming the behavior arises from the bulk of the material, and are not consistent with a composite model with metallic particles separated by an insulating matrix.[27]

Thus, we conclude that the specimens measured here are small-bandgap semiconductors. These bandgaps are much smaller than those observed in most kagomé minerals, but also far from the metallicity observed in materials such as Fe_3Sn_2, $MgCo_6Ge_6$,[28] and KV_3Sb_5,[8−10,29] and place $Ni_3(HIB)_2$ and $Cu_3(HIB)_2$ much farther from the insulating limit than most QSL candidates. It is also interesting to compare our $Ni_3(HIB)_2$ and $Cu_3(HIB)_2$ results to those of other recently discovered kagomé MOFs. Table 1 shows bandgaps for a number of known MOFs.[30−35] The values span a range from metallic and superconducting to >1 eV gap, demonstrating how these MOFs exist in a previously underexplored region of parameter space.

Table 1. Kagomé MOFs with Bandgap and Superconducting Behavior Demonstrating the Diversity of Electrical Conduction in the MOF Kagomé Lattices

kagomé MOF	bandgap (eV)	refs
NiTAA MOF	0.61−1.1	30
(Cu-BHT)	superconducting, T_c = 0.2 K	31,32
NiDT	0.054	33
$Ni_3(HITP)_2$ and $Cu_3(HITP)_2$	0.2	34
$Cu_3(HHTN)_2$	1.6	35

The interplay between the localized transition metal magnetism and the electrical transport can be probed through resistivity measurements as a function of magnetic field, i.e., magnetoresistance measurements. We find only small changes with applied fields above 20 and 120 K for $Ni_3(HIB)_2$ and $Cu_3(HIB)_2$, respectively (Figure 3a,b). While the high resistivity prevents measurements down to the base temperature, we observe the beginning of a modest (∼10%) positive magnetoresistance in both materials below these temperatures, implying some impact of the localized spins on the electrical transport. This also suggests that grain boundary scattering, while assuredly present, is not dominating the observed transport: grain boundary scattering should be independent of the magnetic field. Future work using micro/nanoscale-constrained devices to overcome the high resistivities could further explore this coupling in greater detail.

https://doi.org/10.1021/acs.inorgchem.2c00081
Inorg. Chem. XXXX, XXX, XXX−XXX

Thermodynamic measurements provide further insight into the physical properties of $M_3(HIB)_2$. Figure 4a shows the low-temperature specific heat of $Ni_3(HIB)_2$. The small upturn starting below ~5 K develops into a broad hump below ~1 K. It is likely not an intrinsic magnetic contribution, as the change in entropy is very small (inset of Figure 4a), and is more likely the result of defect spins. Except for that small upturn, we find that the data follow well the behavior expected for a simple mixture of electronic and phononic contributions: $C_p/T = \gamma + \beta_3 T^2$, where $\beta_3 T^3$ represents the phonon contribution and γ a T-linear contribution. This fit gives a β_3 of 4.3(8) mJ mol^{-1} K^{-4} and a γ of 148(4) mJ mol^{-1} K^{-2}. The latter value implies a very large and significant T-linear contribution to the specific heat, which is unexpected for an insulator. Careful inspection shows that this region is not quite linear, which likely means that the contribution is from the spins in the material; e.g., classical spin waves exhibit a T to $T^{3/2}$ dependence. In the quantum spin liquid literature, such behavior is often attributed to the presence of a spin-on continuum, but there are other potential explanations, including the presence of significant structural and/or magnetic glassiness or the existence of a singlet ground state but with a low-lying $S = 1$ excited state. Indeed, careful inspection shows that this region is not quite linear. In addition, if the sample is interpreted as a metal, the γ obtained is much larger than one would expect (by 10−100 times) and would imply a very large effective mass, ~10−100 m_e.[36] Such a large effective mass is uncommon in a metal, as this does not have the ingredients to be a heavy Fermion system, but is known in amorphous Ti_xSi_{100-x} alloys,[37] and suggestive of significant structural disorder.[38,39]

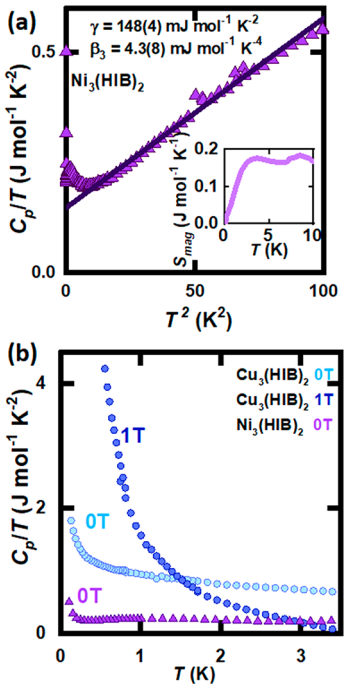

Figure 4. (a) Linear fit of heat capacity divided by temperature (C_p/T) as a function of T^2 for $Ni_3(HIB)_2$ where $C_p/T = \gamma + \beta_3 T^2$, where $\beta_3 T^3$ represents the phonon contribution and γ the Sommerfeld coefficient. The inset shows the change in excess entropy from 0 to 10 K. (b) C_p/T as a function of T, where $Cu_3(HIB)_2$ data at $\mu_o H = 0$ and 1 T are compared to $Ni_3(HIB)_2$ data at $\mu_o H = 0$ T.

In contrast, the low-temperature specific heat of $Cu_3(HIB)_2$ is complex and does not follow simple relations under any measured conditions. The low-temperature heat capacity of $Cu_3(HIB)_2$ (Figure 4b) shows a smooth divergence down to 0.1 K. This divergence contains significant entropy. To explore how much of this entropy arises from magnetism, we also carried out measurements under an applied field. The divergence moves to higher temperatures and becomes more pronounced under the application of a $\mu_o H = 1$ T field, consistent with a primarily magnetic origin. In addition, the magnitude of the change is significant, implying that the behavior at these temperatures is not governed by strong interactions between spins (which would tend to suppress the ability of an applied field to change the magnetic behavior).

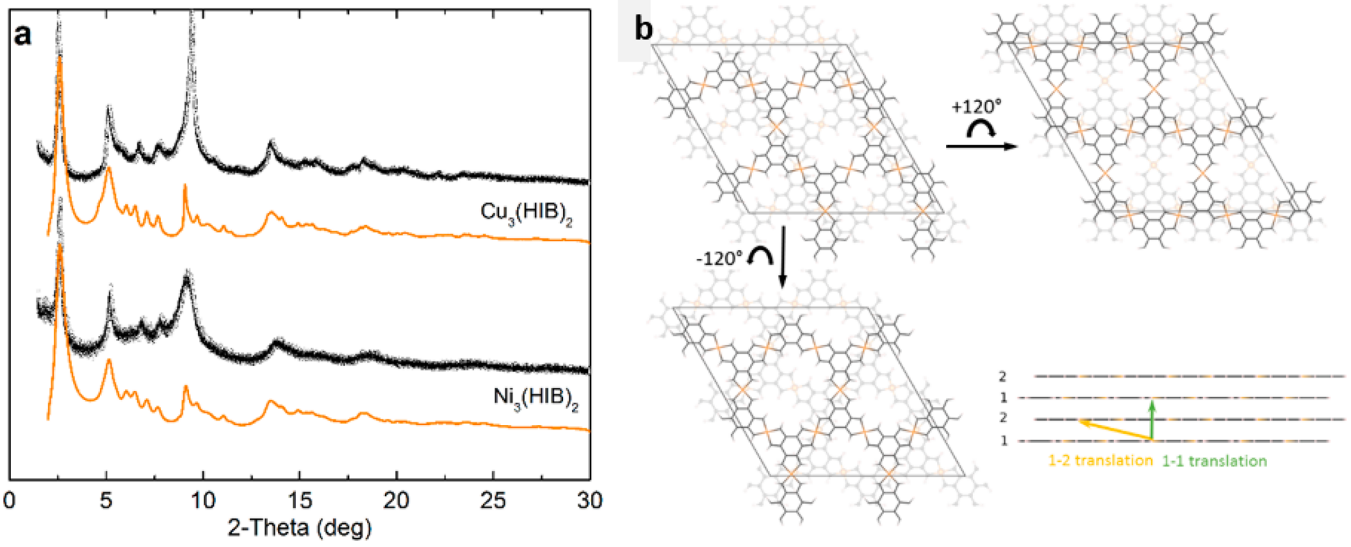

Figure 5. (a) Synchrotron X-ray diffraction data at 100 K (ref 17) compared to the optimal stacking fault models developed in this work (solid lines). (b) Individual layers [$Ni_3(HIB)_2$ shown] can be rotated by 120° and keep the same net interactions with immediately adjacent layers but are distinct in orientation with the next nearest layers. We model the stacking faults as a weighted random distribution of these rotations, combined with static in-plane displacements between nearest (1−2) and next-nearest (1−1) layers.

https://doi.org/10.1021/acs.inorgchem.2c00081
Inorg. Chem. XXXX, XXX, XXX−XXX

Nonetheless, as in the case of $Ni_3(HIB)_2$, no signatures of a phase transition or magnetic order are observed.

To identify the microscopic origins of the observed lack of magnetic order and proximity to metallicity, we carried out a detailed analysis of synchrotron X-ray diffraction data. Powder X-ray diffraction is a sensitive tool for the determination of imperfections in the stacking of layered materials through the characteristic asymmetric broadening and changes in intensities of specific families of Bragg reflections. Figure 5a shows a comparison of synchrotron X-ray diffraction data at 100 K for $Ni_3(HIB)_2$ and $Cu_3(HIB)_2$ (from ref 17) with the previously reported structural model, and the refined stacking fault model developed here. From the measured data, several observations are immediately apparent. (1) Individual Bragg reflections are much broader than that predicted from a perfect crystal structure plus instrumental contributions. (2) There is a pronounced asymmetry in the visible reflections, with pronounced right-side tails for the large reflections at 2θ values of 2.54°, 5.2°, and 13.6° and a left-side tail for that at 9.52°. (3) Some of the peaks in $Ni_3(HIB)_2$ are broader than those in $Cu_3(HIB)_2$, with less resolved fine peak structure.

Observation 1 is indicative of stacking faults in a crystalline material, with observations 2 and 3 constraining the possible models. Because the previous report[17] found evidence of in-plane displacements between adjacent layers, we initially attempted to model these data using variable in-plane displacements, but that was insufficient to explain the data. It could not capture the observed peak asymmetries or the variation in peak structure between the two materials. Inspection of the structure shows another potential source of stacking complexity. Individual layers can be rotated around a 3-fold axis that is, from the perspective of the immediate adjacent layers, equivalent but results in different interactions when considering the longer-range stacking. Thus, we built a model incorporating this potential rotational disorder in addition to interlayer shifts (Figure 5b). When combined with finite size effects, both in plane and a finite (instead of infinite) number of stacked layers, this results in models that capture the key qualitative features of the data. The best found values of the parameters are listed in Table 2. Further refinements to this model adding complexity can improve quantitative agreement but do not change the qualitative characteristics.

Table 2. Iteratively Found Optimal Parameters for the Stacking Fault Model for $Ni_3(HIB)_2$ and $Cu_3(HIB)_2$

	$Ni_3(HIB)_2$	$Cu_3(HIB)_2$
rotational stacking fault probability	0.50	0.37
layer 1 to layer 2 in-plane displacement	(0.4, 0.45)	(0.398, 0.453)
layer 1 to layer 1 in-plane displacement	(0.025, 0.068)	(0.024797, 0.06836)
average in-plane dimension (nm)	80	100
average no. of layers per crystallite	20	100

In light of these significant structural complexities, it is important to identify the likely origins of our observations of magnetic frustration, a lack of magnetic order, and the proximity to metallicity. A lack of magnetic order or other phase transitions and T-linear contributions to specific heat are often taken as quantum spin liquid physics signatures. However, substantial work in recent years has shown how disorder can often present many of the same attributes in the absence of a QSL state and also how disorder might itself enable QSL-type states.[6,7,40−44] For the case of $Cu_3(HIB)_2$, the significant structural disorder, combined with the low in-plane spin density, is expected to prevent the formation of static magnetic order and result in a broad continuum of magnetic entropy at low temperatures, exactly as observed. In contrast to a QSL state, however, a ground state driven by structural disorder should be very sensitive and tunable in an applied magnetic field, also as observed. Thus, we attribute the behaviors of $Cu_3(HIB)_2$ not to QSL physics, but rather to strong disorder.

The situation of $Ni_3(HIB)_2$ is distinct, as there is an additional degree of freedom in play, single ion energy levels. The local crystal field of Ni^{2+} in $Ni_3(HIB)_2$ is square planar, and thus, an $S = 0$ ground state is expected. However, clear $S = 1$ magnetism is observed above 2 K in magnetization. This suggests that there is a very low lying $S = 1$ excited state, which would result in a complex contribution to the specific heat below 2 K that would not be strongly dependent on the field as in disordered amorphous alloys, although a spin contribution (e.g., spin wave-like) is also possible.[37] This explains the salient differences we observe in the low-temperature specific heat relative to $Cu_3(HIB)_2$, and thus, we assign $Ni_3(HIB)_2$ a highly disordered, singlet ground state.

CONCLUSION

Magnetization, heat capacity, and resistivity measurements of $Ni_3(HIB)_2$ and $Cu_3(HIB)_2$ demonstrate that these materials are paramagnets with antiferromagnetic correlations and small, semiconducting band gaps. We observe a 2.5-fold increase in the heat capacity for $Cu_3(HIB)_2$ with $\mu_oH = 1$ T. This trend indicates nearly free spins easily perturbed by an external field and rules out strongly interacting spin liquid physics in this regime. Similarly, for $Ni_3(HIB)_2$, the large T-linear specific heat can be explained by a confluence of a single ion singlet ground state with stacking faults due to the disorder between layers, yet these MOFs are unique in exhibiting both localized magnetism and nearly metallic behavior with a kagomé lattice. If the structural disorder can be suppressed, for example by controlled, layer-by-layer vapor phase synthesis as has been developed for graphene and transition metal dichalcogenides,[45−47] then they have the potential to reveal new physics in the rarely explored regime of semiconducting kagomé lattices. More broadly, these MOFs demonstrate how the development of chemically tunable material platforms can access new regions of magnetic and electronic thermodynamic parameter space.[48]

AUTHOR INFORMATION

Corresponding Author

Tyrel M. McQueen − *Department of Chemistry, Institute for Quantum Matter and Department of Physics and Astronomy, and Department of Materials Science and Engineering, Johns Hopkins University, Baltimore, Maryland 21218, United States;* orcid.org/0000-0002-8493-4630; Email: mcqueen@jhu.edu

Authors

Tanya Berry − *Department of Chemistry and Institute for Quantum Matter and Department of Physics and Astronomy, Johns Hopkins University, Baltimore, Maryland 21218, United States;* orcid.org/0000-0002-1583-2120

https://doi.org/10.1021/acs.inorgchem.2c00081
Inorg. Chem. XXXX, XXX, XXX−XXX

Jennifer R. Morey − *Department of Chemistry and Institute for Quantum Matter and Department of Physics and Astronomy, Johns Hopkins University, Baltimore, Maryland 21218, United States*
Kathryn E. Arpino − *Max Planck Institute for Chemical Physics of Solids, 01187 Dresden, Germany*
Jin-Hu Dou − *Department of Chemistry, Massachusetts Institute of Technology, Cambridge, Massachusetts 02139, United States;* orcid.org/0000-0002-6920-9051
Claudia Felser − *Max Planck Institute for Chemical Physics of Solids, 01187 Dresden, Germany*
Mircea Dincă − *Department of Chemistry, Massachusetts Institute of Technology, Cambridge, Massachusetts 02139, United States*

Complete contact information is available at: https://pubs.acs.org/10.1021/acs.inorgchem.2c00081

Notes

The authors declare no competing financial interest.

■ ACKNOWLEDGMENTS

This work was supported in part by the Institute for Quantum Matter, an Energy Frontier Research Center funded by the U.S. Department of Energy, Office of Science, Office of Basic Energy Sciences, under Grant DE-SC0019331. The dilution refrigerator was funded by the National Science Foundation, Division of Materials Research, Grant 0821005. K.E.A. acknowledges the funding provided by the Alexander von Humboldt Foundation. Work in the Dincă lab was funded by the Army Research Office (Grant W911NF-17-1-0174). The MPMS was funded by the National Science Foundation, Division of Materials Research, Major Research Instrumentation Program, under Grant 1828490.

■ REFERENCES

(1) Huang, X.; Sheng, P.; Tu, Z.; Zhang, F.; Wang, J.; Geng, H.; Zou, Y.; Di, C.-a.; Yi, Y.; Sun, Y.; et al. A Two-Dimensional π-d Conjugated Coordination Polymer with Extremely High Electrical Conductivity and Ambipolar Transport Behaviour. *Nat. Commun.* **2015**, *6*, 7408.
(2) Campbell, M. G.; Liu, S. F.; Swager, T. M.; Dincă, M. Chemiresistive Sensor Arrays from Conductive 2D Metal-Organic Frameworks. *J. Am. Chem. Soc.* **2015**, *137*, 13780−13783.
(3) Clough, A. J.; Yoo, J. W.; Mecklenburg, M. H.; Marinescu, S. C. Two-Dimensional Metal−Organic Surfaces for Efficient Hydrogen Evolution from Water. *J. Am. Chem. Soc.* **2015**, *137*, 118−121.
(4) Ko, M.; Mendecki, L.; Mirica, K. A. Conductive Two-Dimensional Metal−Organic Frameworks as Multifunctional Materials. *Chem. Commun.* **2018**, *54*, 7873−7891.
(5) Broholm, C.; Cava, R. J.; Kivelson, S. A.; Nocera, D. G.; Norman, M. R.; Senthil, T. Quantum Spin Liquids. *Science* **2020**, *367*, No. eaay0668.
(6) Chamorro, J. R.; McQueen, T. M.; Tran, T. T. Chemistry of quantum spin liquids. *Chem. Rev.* **2021**, *121*, 2898−2934.
(7) Knolle, J.; Moessner, R. A Field Guide to Spin Liquids. *Annu. Rev. Condens. Matter Phys.* **2019**, *10*, 451.
(8) Kida, T.; Fenner, L. A.; Dee, A. A.; Terasaki, I.; Hagiwara, M.; Wills, A. S. The giant anomalous Hall effect in the ferromagnet Fe_3Sn_2-a frustrated kagome metal. *J. Phys.: Condens. Matter* **2011**, *23*, 112205.
(9) Ye, L.; Kang, M.; Liu, J.; Von Cube, F.; Wicker, C. R.; Suzuki, T.; Jozwiak, C.; Bostwick, A.; Rotenberg, E.; Bell, D. C.; Fu, L.; Comin, R.; Checkelsky, J. G. Massive Dirac Fermions in a Ferromagnetic Kagome Metal. *Nature* **2018**, *555*, 638−642.
(10) Yang, S.-Y.; Wang, Y.; Ortiz, B. R.; Liu, D.; Gayles, J.; Derunova, E.; Gonzalez-Hernandez, R.; Šmejkal, L.; Chen, Y.; Parkin, S. S. P.; Wilson, S. D.; Toberer, E. S.; McQueen, T.; Ali, M. N. Giant, Unconventional Anomalous Hall effect in the Metallic Frustrated Magnet Candidate, KV_3Sb_5. *Sci. Adv.* **2020**, *6*, No. eabb6003.
(11) Ortiz, B. R.; Gomes, L. C.; Morey, J. R.; Winiarski, M.; Bordelon, M.; Mangum, J. S.; Oswald, I. W. H.; Rodriguez-Rivera, J. A.; Neilson, J. R.; Wilson, S. D.; Ertekin, E.; McQueen, T. M.; Toberer, E. S. New Kagome Prototype Materials: Discovery of KV_3Sb_5, RbV_3Sb_5, and CsV_3Sb_5. *Phys. Rev. Materials* **2019**, *3*, No. 094407.
(12) Wang, Y.; Yang, S. Y.; Sivakumar, P. K.; Ortiz, B. R.; Teicher, S. M. L.; Wu, H.; Srivastava, A. K.; Garg, C.; Liu, D.; Parkin, S. S. P.; Toberer, E. S.; McQueen, T. M.; Wilson, S. D.; Ali, M. N. Proximity-induced spin-triplet superconductivity and edge supercurrent in the topological Kagome metal, $K_{1-x}V_3Sb_5$. *arXiv* **2020**, DOI: 10.48550/arXiv.2012.05898.
(13) Ortiz, B. R.; Sarte, P. M.; Kenney, E. M.; Graf, M. J.; Teicher, S. M. L.; Seshadri, R.; Wilson, S. D. Superconductivity in the Z2 kagome metal KV_3Sb_5. *Phys. Rev. Mater.* **2021**, *5*, No. 034801.
(14) Shumiya, N.; Hossain, M. S.; Yin, J.-X.; Jiang, Y.-X.; Ortiz, B. R.; Liu, H.; Shi, Y.; Yin, Q.; Lei, H.; Zhang, S. S.; Chang, G.; Zhang, Q.; Cochran, T. A.; Multer, D.; Litskevich, M.; Cheng, Z.-J.; Yang, X. P.; Guguchia, Z.; Wilson, S. D.; Hasan, M. Z. Intrinsic nature of chiral charge order in the kagome superconductor RbV_3Sb_5. *Phys. Rev. B* **2021**, *104*, No. 035131.
(15) Anderson, P. W. The Resonating Valence Bond State in La_2CuO_4 and Superconductivity. *Science* **1987**, *235*, 1196−1198.
(16) Kelly, Z. A.; Gallagher, M. J.; McQueen, T. M. Electron Doping a Kagome Spin Liquid. *Phys. Rev. X* **2016**, *6*, 041007.
(17) Dou, J.-H.; Sun, L.; Ge, Y.; Li, W.; Hendon, C. H.; Li, J.; Gul, S.; Yano, J.; Stach, E. A.; Dinca, M. Signature of Metallic Behavior in the Metal-Organic Frameworks M_3(hexaiminobenzene)$_2$ (M = Ni, Cu). *J. Am. Chem. Soc.* **2017**, *139*, 13608−13611.
(18) Tiana, D.; Hendon, C. H.; Walsh, A. Ligand design for long-range magnetic order in metal-organic frameworks. *Chem. Commun.* **2014**, *50*, 13990−3.
(19) Treacy, M. M., Jr.; Deem, M. W.; Newsam, J. M. *DIFFaX* (https://www.public.asu.edu/~mtreacy/DIFFaX.html) (accessed 09-01-2021).
(20) McQueen, T. M.; Elbert, D. *Materials, Automated* (https://www.materialsautomated.com) (accessed 11-01-2021).
(21) Hjorth Larsen, A.; et al. The atomic simulation environment − A Python library for working with atoms. *J. Phys.: Condens. Matter* **2017**, *29*, 273002.
(22) Sheberla, D.; Sun, L.; Blood-Forsythe, M. A.; Er, S.; Wade, C. R.; Brozek, C. K.; Aspuru-Guzik, A.; Dinca, M. High Electrical Condutivity in Ni3(2,3,6,7,10,11-Hexaiminotriphen-ylene)$_2$, a Semiconducting Metal − Organic Graphene Analogue. *J. Am. Chem. Soc.* **2014**, *136*, 8859−8862.
(23) Clough, A. J.; Skelton, J. M.; Downes, C. A.; De La Rosa, A. A.; Yoo, J. W.; Walsh, A.; Melot, B. C.; Marinescu, S. C. Metallic Conductivity in a Two-Dimensional Cobalt Dithiolene Metal-Organic Framework. *J. Am. Chem. Soc.* **2017**, *139*, 10863−10867.
(24) Usman, M.; Mendiratta, S.; Lu, K. L. Semiconductor Metal Organic Frameworks: Future Low-Bandgap Materials. *Adv. Mater.* **2017**, *29*, 1605071.
(25) Kobayashi, Y.; Jacobs, B.; Allendorf, M. D.; Long, J. R. Conductivity, Doping, and Redox Chemistry of a Microporous Dithiolene-Based Metal−Organic Framework. *Chem. Mater.* **2010**, *22*, 4120−4122.
(26) Vladimirov, I.; Kühn, M.; Geßner, T.; May, F.; Weitz, R. T. Energy Barriers at Grain Boundaries Dominate Charge Carrier Transport in an Electron-Conductive Organic Semiconductor. *Sci. Rep.* **2018**, *8*, 14868.
(27) Mclachlan, D. S.; Blaszkiewicz, M.; Newnham, R. E. Electrical Resistivity of Composites. *J. Am. Ceram. Soc.* **1990**, *73*, 2187−2203.
(28) Sinha, M.; Vivanco, H. K.; Wan, C.; Siegler, M. A.; Stewart, V. J.; Pogue, E. A.; Pressley, L. A.; Berry, T.; Wang, Z.; Johnson, I.;

Chen, M.; Tran, T. T.; Phelan, W. A.; McQueen, T. M. Twisting of 2D Kagomé Sheets in Layered Intermetallics. *ACS Cent. Sci.* **2021**, *7* (8), 1381−1390.
(29) Jiang, Y. X.; Yin, J. X.; Denner, M. M.; Shumiya, N.; Ortiz, B. R.; Xu, G.; Guguchia, Z.; He, J.; Hossain, M. S.; Liu, X.; Ruff, J.; Kautzsch, L.; Zhang, S. S.; Chang, G.; Belopolski, I.; Zhang, Q.; Cochran, T. A.; Multer, D.; Litskevich, M.; Cheng, Z. J.; Yang, X. P.; Wang, Z.; Thomale, R.; Neupert, T.; Wilson, S. D.; Hasan, M. Z. Unconventional chiral charge order in kagome superconductor KV3Sb5. *Nat. Mater.* **2021**, *20*, 1353.
(30) Jiang, Y.; Oh, I.; Joo, S. H.; Buyukcakir, O.; Chen, X.; Lee, S. H.; Huang, M.; Seong, W. K.; Kwak, S. K.; Yoo, J.-W.; et al. Partial Oxidation-Induced Electrical Conductivity and Paramagnetism in a Ni(II) Tetraaza[14]Annulene-Linked Metal Organic Framework. *J. Am. Chem. Soc.* **2019**, *141*, 16884−16893.
(31) Huang, X.; Zhang, S.; Liu, L.; Yu, L.; Chen, G.; Xu, W.; Zhu, D. Superconductivity in a Copper(II)-Based Coordination Polymer with Perfect Kagome Structure. *Angew. Chem., Int. Ed.* **2018**, *57*, 146−150.
(32) Takenaka, T.; Ishihara, K.; Roppongi, M.; Miao, Y.; Mizukami, Y.; Makita, T.; Tsurumi, J.; Watanabe, S.; Takeya, J.; Yamashita, M.; et al. Strongly correlated superconductivity in a copper-based metalorganic framework with a perfect kagome lattice. *Sci. Adv.* **2021**, *7*, eebf3996.
(33) Song, X.; Liu, J.; Zhang, T.; Chen, L. 2D Conductive Metal-Organic Frameworks for Electronics and Spintronics. *Sci. China Chem.* **2020**, *63*, 1391.
(34) Chen, S.; Dai, J.; Zeng, X. C. Metal−Organic Kagome Lattices M3(2,3,6,7,10,11-Hexaiminotriphenylene)2 (M = Ni and Cu): From Semiconducting to Metallic by Metal Substitution. *Phys. Chem. Chem. Phys.* **2015**, *17*, 5954−5958.
(35) Meng, Z.; Mirica, K. A. Two-dimensional d-π conjugated metal-organic framework based on hexahydroxytrinaphthylene. *Nano Res.* **2021**, *14* (2), 369−375.
(36) Cottingham, P.; Miller, D. C.; Sheckelton, J. P.; Neilson, J. R.; Feygenson, M.; Huq, A.; McQueen, T. M. Dynamic Charge Disproportionation in the 1D Chain Material PdTeI. *J. Mater. Chem. C* **2014**, *2*, 3238−3246.
(37) Rogatchev, A. Y.; Mizutani, U. Hopping conductivity and specific heat in insulating amorphous alloys. *Phys. Rev. B* **2000**, *61*, 15550.
(38) Xie, J.; Zhang, H.; Li, S.; Wang, R.; Sun, X.; Zhou, M.; Zhou, J.; Lou, X. W.; Xie, Y. Defect-Rich MoS2 Ultrathin Nanosheets with additional Active Edge Sites for Enhanced Electrocatalytic Hydrogen Evolution. *Adv. Mater.* **2013**, *25*, 5807−5813.
(39) Shi, H.; Barker, J.; Saïdi, M. Y.; Koksbang, R.; Morris, L. Graphite structure and lithium intercalation. *J. Power Sources* **1997**, *68*, 291−295.
(40) Wen, J.-J.; Koohpayeh, S. M.; Ross, K. A.; Trump, B. A.; McQueen, T. M.; Kimura, K.; Nakatsuji, S.; Qiu, Y.; Pajerowski, D. M.; Copley, J. R. D.; Broholm, C. L. Disordered Route to the Coulomb Quantum Spin Liquid: Random Transverse Fields on Spin Ice in $Pr_2Zr_2O_7$. *Phys. Rev. Lett.* **2017**, *118*, 107206.
(41) Arpino, K. E.; Trump, B. A.; Scheie, A. O.; McQueen, T. M.; Koohpayeh, S. M. Impact of Stoichiometry of Yb2Ti2O7 on its Physical Properties. *Phys. Rev. B: Condens. Matter Mater. Phys.* **2017**, *95*, No. 094407.
(42) Morey, J.; Plumb, K.; Pasco, C.; Trump, B.; McQueen, T.; Koohpayeh, S. Growth and characterization of iron scandium sulfide $FeSc_2S_4$. *J. Cryst. Growth* **2016**, *454*, 128−133.
(43) Syzranov, S. V.; Ramirez, A. P. Hidden energy scale in geometrically frustrated systems: are quantum spin liquids achievable? *arXiv* **2021**, 2105.08070.
(44) Zhu, Z.; Maksimov, P. A.; White, S. R.; Chernyshev, A. L. Disorder-Induced Mimicry of a Spin Liquid in $YbMgGaO_4$. *Phys. Rev. Lett.* **2017**, *119*, 157201.
(45) Castellanos-Gomez, A.; Barkelid, M.; Goossens, A. M.; Calado, V. E.; van der Zant, H. S.; Steele, G. A. Laser-Thinning of MoS2: On Demand Generation of a Single-Layer Semiconductor. *Nano Lett.* **2012**, *12*, 3187−3192.
(46) Eda, G.; Yamaguchi, H.; Voiry, D.; Fujita, T.; Chen, M.; Chhowalla, M. Photoluminescence from Chemically Exfoliated MoS2. *Nano Lett.* **2011**, *11*, 5111−5116.
(47) Claire, F. J.; Solomos, M. A.; Kim, J.; Wang, G.; Siegler, M. A.; Crommie, M. F.; Kempa, T. J. Structural and electronic switching of a single crystal 2D metal-organic framework prepared by chemical vapor deposition. *Nat. Commun.* **2020**, *11* (1), 5524.
(48) McQueen, T. M.; Chamorro, J.; Ghasemi, A.; Phelan, W. A.; Pogue, L.; Pressley, M.; Sinha, M.; Stewart, V.; Tran, T. T.; Vivanco, H.; Winiarski, M. Future Directions in Quantum Materials Synthesis. In *Fundamentals of Quantum Materials: A Practical Guide to Synthesis and Exploration*; January 2021; ISBN: 978-981-121-936-8.

https://doi.org/10.1021/acs.inorgchem.2c00081
Inorg. Chem. XXXX, XXX, XXX−XXX